

2001-2022 global gross primary productivity dataset using an ensemble model based on random forest

Xin Chen¹, Tiexi Chen^{1,2,3*}, Xiaodong Li⁴, Yuanfang Chai⁵, Shengjie Zhou¹, Renjie Guo⁶, Jie Dai¹

¹School of Geographical Sciences, Nanjing University of Information Science and Technology, Nanjing 210044, Jiangsu, China.

²Qinghai Provincial Key Laboratory of Plateau Climate Change and Corresponding Ecological and Environmental Effects, Qinghai University of Science and Technology, Xining 810016, China

³School of Geographical Sciences, Qinghai Normal University, Xining 810008, Qinghai, China.

⁴Qinghai Institute of Meteorological Science, Xining 810008, Qinghai, China.

⁵Department of Earth Sciences, Vrije Universiteit Amsterdam, Boelelaan 1085, 1081 HV, Amsterdam, the Netherlands

⁶Faculty of Geographical Science, Beijing Normal University, Beijing, China.

Correspondence to: Tiexi Chen (txchen@nuist.edu.cn)

Abstract. Advancements in remote sensing technology have significantly contributed to the improvement of models for estimating terrestrial gross primary productivity (GPP). However, discrepancies in the spatial distribution and interannual variability within GPP datasets pose challenges to a comprehensive understanding of the terrestrial carbon cycle. In contrast to previous models that rely on remote sensing and environmental variables, we developed an ensemble model based on the random forest (ERF model). This model used GPP outputs from established models (EC-LUE, GPP-kNDVI, GPP-NIRv, Revised-EC-LUE, VPM, MODIS) as inputs to estimate GPP. The ERF model demonstrated superior performance, explaining 85.1% of the monthly GPP variations at 170 sites, surpassing the performance of selected GPP models (67.7%-77.5%) and an independent random forest model using remote sensing and environmental variables (81.5%). Additionally, the ERF model improved accuracy across each month and various subvalues, mitigating the issue of "high value underestimation and low value overestimation" in GPP estimates. Over the period from 2001 to 2022, the global GPP estimated by the ERF model was 132.7 PgC yr⁻¹, with an increasing trend of 0.42 PgC yr⁻², which was comparable to or slightly better than the accuracy of other mainstream GPP datasets in term of validation results of GPP observations independent of FLUXNET (ChinaFlux). Importantly, for the growing number of GPP datasets, our study provides a way to integrate these GPP datasets, which may lead to a more reliable estimate of global GPP.

31 **1 Introduction**

32 Gross primary productivity (GPP) is the largest carbon flux in the global carbon cycle, and serves as the primary input of
33 carbon into the terrestrial carbon cycle. Uncertainties in GPP estimates can propagate to other carbon flux estimates, making
34 it crucial to clarify the spatio-temporal patterns of GPP (Ruehr et al., 2023; Xiao et al., 2019). However, global GPP is
35 variously estimated from 90 PgC yr⁻¹ to 160 PgC yr⁻¹ across different studies, with these variations becoming more
36 pronounced when scaled down to regional scales or specific ecosystem types (Anav et al., 2015; Jung et al., 2020; Ryu et al.,
37 2019). This variability underscores the necessity for innovative methods to reduce uncertainty in GPP estimates.

38 The light use efficiency (LUE) model is one of the most widely adopted methods for estimating GPP. It assumes that GPP is
39 proportional to the photosynthetically active radiation absorbed by vegetation, and optimizes the spatio-temporal pattern of
40 GPP through meteorological constraints such as temperature and moisture (Pei et al., 2022). However, variations in these
41 constraints varies significantly, leading to differences of over 10% in model explanatory power. (Yuan et al., 2014). Recent
42 studies have proposed some novel vegetation indices that have been shown to be effective proxies for GPP through
43 theoretical derivation and observed validation (Badgley et al., 2017; Camps-Valls et al., 2021). However, these vegetation
44 indices often use only remote sensing data as an input for estimating long-term GPP without considering meteorological
45 factors, which has led to some controversy (Chen et al., 2024; Dechant et al., 2022; Dechant et al., 2020). Both LUE and
46 vegetation index models use linear mathematical formulas to estimate GPP, but ecosystems are inherently complex, and the
47 biases introduced by these numerical models increase the uncertainty of GPP estimates. Machine learning models have
48 shown great potential for improving GPP estimates in previous studies (Guo et al., 2023; Jung et al., 2020). These models
49 are trained by non-physical means directly using GPP observations and selected environmental and vegetation variables, and
50 the performance of the models depends on the number and quality of observed data and the representativeness of input data.
51 Nevertheless, direct validation from flux towers of FLUXNET reveals that these models typically explain only about 70% of
52 monthly GPP variations, with similar performance to other GPP estimate models (Badgley et al., 2019; Jung et al., 2020;
53 Wang et al., 2021; Zheng et al., 2020). Due to deviations in the model structure, a common limitation across these models is
54 the poor estimate of monthly extreme GPP, leading to the phenomenon of "high value underestimation and low value
55 overestimation " (Zheng et al., 2020). Especially for extremely high values, which usually occur during the growing season
56 and largely determine the annual totals and interannual fluctuations of GPP, this underestimation may hinder our
57 understanding of the global carbon cycle.

58 It is challenging for a single model to provide accurate estimates for all global regions. Previous studies have shown that
59 ensemble models perform significantly better than single models and can handle some inherent issues in single models
60 (Chen et al., 2020; Yao et al., 2014). Traditional multi-model ensemble methods usually use a simple multi-model average or
61 a Bayesian model averaging. However, these methods typically assign fixed weights to each model and are essentially linear
62 combinations. Recent studies have incorporated machine learning techniques to multi-model ensembles to establish
63 nonlinear relationships between multiple simulated target variables and real target variable, improving simulation

64 performance (Bai et al., 2021; Tian et al., 2023; Yao et al., 2017). Whether this method can improve some common
65 problems with individual GPP estimate models, such as high value underestimation and low value overestimation, is not
66 clear and needs to further investigation.

67 In this study, we attempt to use an ensemble model based on the random forest (ERF model) to improve global GPP estimate.
68 Specifically, the work of this study includes the following: (1) Recalibrating parameters for each model, and comparing the
69 performance of six GPP estimate models and the ERF model; (2) Focusing on the phenomenon of “high value
70 underestimation and low value overestimation” in each model, and evaluating the performance of each model across
71 different months, vegetation types and subvalues (high value, median value, low value); (3) Developing a global GPP dataset
72 using the ERF model and validating its generalization using GPP observations from ChinaFlux.

73 2 Method

74 2.1 Data at the global scale

75 In this study, we selected remote sensing data from the Moderate Resolution Imaging Spectroradiometer (MODIS) and
76 meteorological data from EAR5 to estimate global GPP (Hersbach et al., 2020). For the remote sensing data, surface
77 reflectance (red band, near infrared band, blue band and shortwave infrared band), leaf area index (LAI) and fraction of
78 photosynthetically active radiation (FPAR) were used. For meteorological data, we selected average air temperature, dew
79 point temperature, minimum air temperature, total solar radiation and direct solar radiation. Dew point temperature and
80 average air temperature were used to calculate saturated vapor pressure difference (VPD) (Yuan et al., 2019), and diffuse
81 solar radiation (DifSR) was derived as the difference between total solar radiation and direct solar radiation. Minimum air
82 temperature was obtained from the hourly air temperature. CO₂ data were obtained from the monthly average carbon dioxide
83 levels measured by the Mauna Loa Observatory in Hawaii. Table 1 provides an overview of the datasets used in this study.

84

85 **Table 1.** Overview of the datasets used in this study.

Variable	Dataset	Spatial resolution	Temporal resolution	Temporal coverage
Surface reflectance (red band and near infrared band)	MCD43C4	0.05°	daily	2001-2022
Surface reflectance (red band, near infrared band, blue band and shortwave infrared band)	MOD09CMG	0.05°	daily	2001-2022
LAI	MOD15A2H	500m	8d	2001-2022
FPAR	MOD15A2H	500m	8d	2001-2022
Average air temperature (AT)	ERA5-land	0.1°	Monthly	2001-2022

Dew point temperature (DPT)	ERA5-land	0.1°	Monthly	2001-2022
Minimum air temperature (MINT)	ERA5-land	0.1°	Monthly	2001-2022
Total solar radiation (TSR)	ERA5 monthly data on single levels	0.25°	Monthly	2001-2022
Direct solar radiation (DirSR)	ERA5 monthly data on single levels	0.25°	Monthly	2001-2022
CO ₂	NOAA's Earth System Research Laboratory	/	Monthly	2001-2022
Distribution map of C4 crops	Harvested Area and Yield for 175 Crops	1/12°	Annual	2000
Land use	MCD12C1	0.05°	Annual	2010

86

87 Previous studies have shown that the photosynthetic capacity of C4 crops is much higher than that of C3 crops (Chen et al.,
88 2014; Chen et al., 2011), so it is necessary to divide the cropland into C3 crops and C4 crops. To estimate the global GPP,
89 we used the "175 Crop harvested Area and yield" dataset, which describes the global harvested area and yield of 175 crops in
90 2000 (Monfreda et al., 2008). We extracted the sum of the area ratios of all C4 crops (corn, corn feed, sorghum, sorghum
91 feed, sugarcane, millet) at each grid as the coverage of C4 crops (Figure S1). Consequently, the estimated value of cropland
92 GPP can be expressed as: coverage of C3 crops × simulated GPP value of C3 crops + coverage of C4 crops × simulated GPP
93 value of C4 crops, which has been used in a previous study (Guo et al., 2023).

94 The land use map was derived from the IGBP classification of MCD12C1, and 2010 was chosen as the reference year (that is,
95 land use data is unchanged in the simulation of global GPP). In order to meet the requirements of subsequent research, land
96 use types were grouped into 9 categories: Deciduous Broadleaf Forest (DBF), Evergreen Needleleaved Forest (ENF),
97 Evergreen Broadleaf Forest (EBF), Mixed Forest (MF), Grassland (GRA), Cropland (including CRO-C3 and CRO-C4),
98 Savannah (SAV), Shrub (SHR), Wetland (WET).

99 Finally, for higher resolution data, we gridded the dataset to 0.05° by averaging all pixels whose center fell within each
100 0.05° grid cell for upscaling. For lower resolution data, we used the nearest neighbor resampling method to 0.05°. In
101 addition, MODIS data were aggregated to a monthly scale to ensure spatio-temporal consistency.

102 **2.2 Observation data at the site scale**

103 GPP observations were sourced from the FLUXNET 2015 dataset, which includes carbon fluxes and meteorological
104 variables from more than 200 flux sites around the world (Pastorello et al., 2020). GPP cannot be obtained directly from flux
105 sites and usually needs to be obtained by dismantling the net ecosystem exchange. We chose a monthly level GPP based on
106 the nighttime partitioning method and retained only high quality data ($NEE_VUT_REF_QC > 0.8$) for every year, ultimately
107 selecting 170 sites with 10932 monthly values for this study (Figure S2). In addition, we selected monthly average air
108 temperature, total solar radiation and VPD. The site observations do not provide direct solar radiation, so we extracted data
109 from ERA5 covering the flux tower. Monthly minimum air temperature was derived from hourly air temperature. Since
110 some required data in GPP simulation are not directly available at flux sites, LAI and FPAR were extracted from
111 MOD15A2H (500 m), and surface reflectance data (red band, near infrared band, blue band and shortwave infrared band)
112 were derived from MCD43A4 (500 m) and MOD09A1 (500 m). These data are roughly similar to the footprint of the flux
113 site and can represent the land surface of the flux site (Chu et al., 2021).

114 **2.3 GPP estimate model**

115 We selected six independent models to estimate GPP in this study. These models are widely used with few model parameters
116 and have demonstrated reliable accuracy in previous studies (Badgley et al., 2017; Zhang et al., 2017; Zheng et al., 2020).
117 The six models are EC-LUE, Revised-EC-LUE, NIRv-based linear model, kNDVI-based linear model, VPM, MODIS. The
118 VPM, MODIS and EC-LUE are LUE models based on remote sensing data and meteorological data (Running et al., 2004;
119 Xiao et al., 2004; Yuan et al., 2007). Zheng et al., (2020) proposed the Revised-EC-LUE model, which divides the canopy
120 into sunlit and shaded leaves, improving the estimate of global GPP (Zheng et al., 2020). The NIRv and kNDVI are novel
121 vegetation indices calculated from the red and near-infrared bands of the reflectance spectrum (Badgley et al., 2017;
122 Camps-Valls et al., 2021). Similar to solar induced chlorophyll fluorescence, they exhibit a linear relationship with GPP and
123 are considered effective proxies for GPP. Detailed descriptions of all models can be found in Text S1.

124 To reduce uncertainty in GPP estimates from a single model, we used the ERF model, the basic idea of which is to
125 restructure the simulated values of multiple models. In this study, we directly used the ERF model to establish the
126 relationship between the GPP simulated by the above six models and GPP observations. In addition, for comparison with the
127 ERF model, we also used the random forest (RF) method for modeling. In this study, we used average air temperature,
128 minimum air temperature, VPD, direct solar radiation, diffuse solar radiation, FPAR and LAI as explanatory variables. Both
129 models used the random forest method, which has been widely used in previous studies of GPP estimate (Guo et al., 2023;
130 Jung et al., 2020). Random forest is an ensemble learning algorithm that combines the outputs of multiple decision trees to
131 produce a single result, and is commonly used for classification and regression problems (Belgiu and Drăguț, 2016). In the
132 regression problem, the output result of each decision tree is a continuous value, and the average of all decision tree outputs
133 is taken as the final result. An overview of all models used can be found in Table 2.

134 **Table 2.** Overview of the models used in this study.

ID	Model	Input data	Output
1	EC-LUE	FPAR, VPD, AT, SRAD, CO ₂	GPP _{EC}
2	Revised-EC-LUE	LAI, VPD, AT, DifSR, DirSR, CO ₂	GPP _{REC}
3	kNDVI-GPP	Red band and near infrared band (MCD43)	GPP _{kNDVI}
4	NIRv-GPP	Red band and near infrared band (MCD43)	GPP _{NIRv}
5	VPM	Red band, near infrared band, blue band, shortwave infrared band (MOD09), AT, SRAD	GPP _{VPM}
6	MODIS	FPAR, SRAD, MINT, VPD	GPP _{MODIS}
7	Random forest model (RF)	LAI, FPAR, AT, MINT, VPD, DifSR, DirSR	GPP _{RF}
8	Ensemble model based on random forest (ERF)	GPP _{EC} , GPP _{REC} , GPP _{kNDVI} , GPP _{NIRv} , GPP _{MODIS} , GPP _{VPM}	GPP _{ERF}

135

136 2.4 Model parameter calibration and validation

137 FLUXNET only provides GPP observations and meteorological data, lacking direct measurements for LAI, FPAR, and
 138 surface reflectance, so remote sensing data is needed. Considering the variety of remote sensing data sources, such as
 139 MODIS and AVHRR, it is evident that calibrating the same GPP estimate model with different remote sensing data can yield
 140 varied parameters. In addition, the number of sites used to calibrate model parameters is also an important influencing factor
 141 for model parameters. The original parameters of these models were calibrated with only a limited number of sites (e.g., 95
 142 sites for Revised EC-LUE model and 104 for NIRv-GPP) (Wang et al., 2021; Zheng et al., 2020). Therefore, to reduce the
 143 impact of the uncertainty of model parameters on simulation results, we did not use original parameters and conducted
 144 parameter calibration for GPP estimate models across different vegetation types. For EC-LUE, Revised EC-LUE, VPM and
 145 MODIS, the Markov chain Monte Carlo method was used to calibrate model parameters. Traditionally, the mean of the
 146 posterior distribution of parameters is taken as the optimal value. However, previous studies have indicated that some model
 147 parameters are not well constrained when calibrating multiple model parameters (Wang et al., 2017; Xu et al., 2006), so we
 148 selected the parameter with the smallest root-mean-square error (RMSE) as the optimal parameter in each iteration. For each
 149 vegetation type, we randomly selected 70% of the data for parameter calibration, and repeated the process 200 times. In
 150 order to avoid overfitting, we adopted the mean of the 200 calibrated parameters as the final model parameters. Similarly, for
 151 the two vegetation index models, we randomly selected 70% of the data in each vegetation type for parameter calibration,
 152 repeating the process 200 times and using the mean of the 200 calibrated parameters as the final model parameters.

153 After obtaining GPP estimates from the six GPP models, we evaluated the simulation performance of the RF model and the
154 ERF model respectively. For both models, we evaluated the model performance using 5-fold-cross-validation, where the
155 process was repeated 200 times, and the mean of the 200 GPP estimates was considered the final GPP estimate. In addition,
156 we used a second validation method in which all data from 70% of the sites were selected for modeling and only all data
157 from the remaining 30% of the sites were validated, a process that was repeated 200 times. This validation will further
158 illustrate the generalization of the model, i.e. its potential for estimating GPP without local observations. We utilized the
159 determination coefficient (R^2) and RMSE as metrics to evaluate the simulation performance of all models. Additionally, we
160 used the ratio of GPP simulations to GPP observations (Sim/Obs) to measure whether the model overestimates or
161 underestimates.

162 **2.5 Global GPP estimate based on ERF model and its uncertainty.**

163 Based on the ERF model, we estimated global GPP for 2001-2022 (ERF_GPP). It is important to note that in this process,
164 we used all the site data to build the model. The uncertainties of ERF_GPP can be attributed to two primary factors: the
165 influence of the number of GPP observations and the influence of the number of features (that is, the simulated GPP). For
166 the first type of uncertainty, we randomly selected 80% of the data to build a model and simulated the multi-year average of
167 global GPP. The process was repeated 100 times, yielding 100 sets of multi-year averages of ERF_GPP. Their standard
168 deviations were considered as the uncertainty of ERF_GPP caused by the number of GPP observations. For the second type
169 of uncertainty, we selected different number of features to build a model and simulated the multi-year average of global GPP.
170 A total of 56 sets of multi-year averages of ERF_GPP were obtained. The standard deviation of different combinations was
171 considered to be the uncertainty of ERF_GPP caused by the number of features.

172 **2.6 Evaluation of the generalization of different GPP datasets**

173 The majority of flux sites in FLUXNET are concentrated in Europe and North America, it is unclear whether the different
174 GPP estimate methods are suitable for regions with sparse flux sites. Recently, ChinaFlux has published GPP observations
175 from several sites, offering an opportunity to evaluate the generalization of different GPP datasets. However, the spatial
176 resolution of most GPP datasets is 0.05° , and a direct comparison with GPP observations at flux sites is challenging.
177 Therefore, we extracted 0.05° MODIS land use covering the flux sites. If the vegetation type of the flux site matched the
178 MODIS land use, the site was used for the analysis. Finally, a total of 12 flux sites were selected (Figure S2), and Table S1
179 shows the information of these sites. The same procedure was applied to FLUXNET, resulting in the selection of 52 sites. It
180 should be noted that due to the absence of meteorological data from some sites in Chinaflux, we did not validate all GPP
181 estimate models at the site scale (500 m).

182 We evaluated the generalization of ERF_GPP at 12 ChinaFlux sites and 52 FLUXNET sites. In addition, we selected a
183 number of widely used GPP datasets for comparison, including BESS (Li et al., 2023), GOSIF (Li and Xiao, 2019),
184 FLUXCOM: random forest-based version (FLUXCOM-RF) and ensemble version (FLUXCOM-ENS) (Jung et al., 2020),

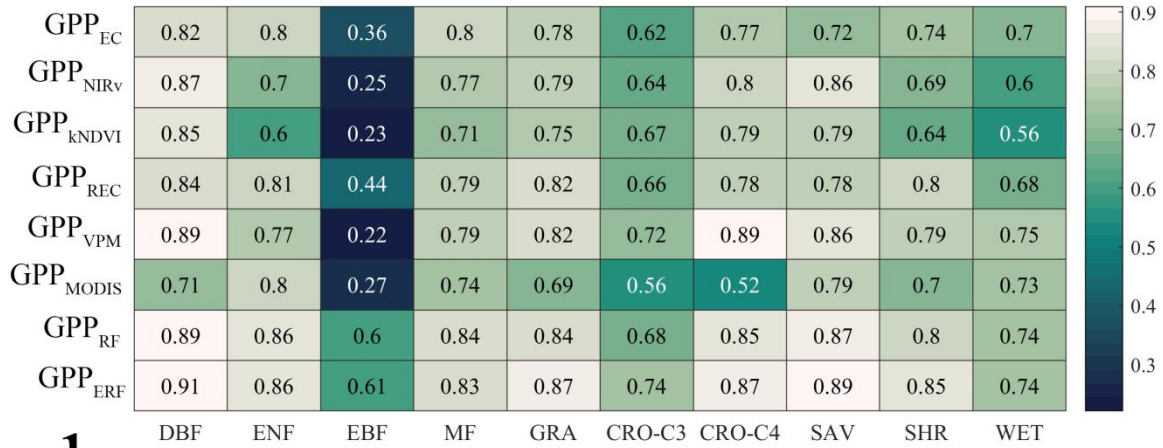
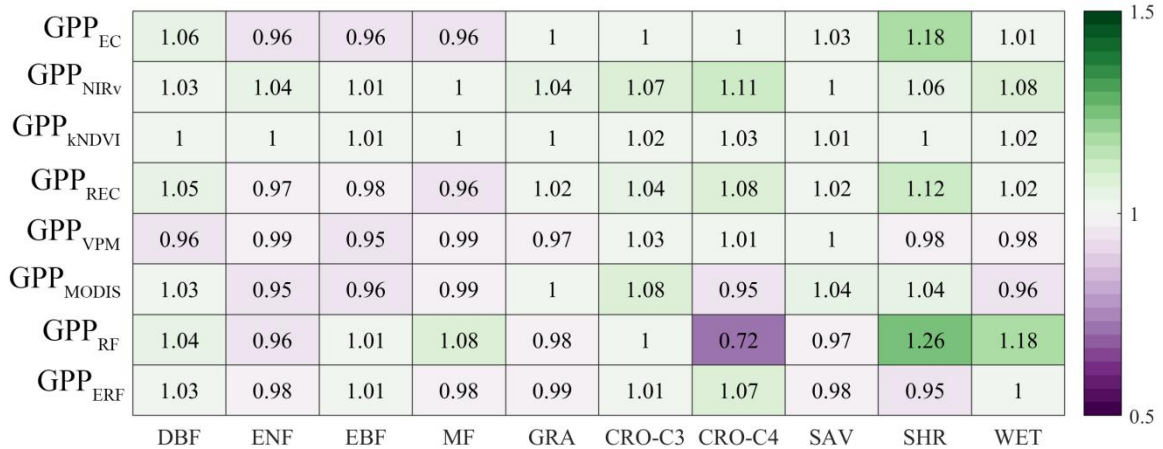
185 NIRv (Wang et al., 2021), Revise-EC-LUE (Zheng et al., 2020), MODIS (Running et al., 2004), VPM (Zhang et al., 2017),
186 which were generated using different GPP estimate methods. These GPP datasets all have a spatial resolution of 500 m-0.5°,
187 similar to the resampling process in section 2.1, we have unified them to 0.05°. The common time range for these datasets
188 spanned from 2001 to 2018, and the temporal resolution was unified to monthly to match the GPP observations.

189 **3 Result**

190 **3.1 Performance of GPP estimate models at site scale**

191 Table S2-S7 show the optimization results of the six GPP estimate model parameters. Consistent with previous study, in the
192 Revised EC-LUE model, the light use efficiency parameter of shade leaves was significantly higher than that of sunlit leaves
193 (Zheng et al., 2020). It is necessary to divide cropland into C3 crops and C4 crops. In all models, the light use efficiency
194 parameters of C4 crops were significantly higher than those of C3 crops, which was particularly reflected in the two
195 vegetation index models of GPP_{kNDVI} and GPP_{NIRv} , the slope of the linear regression directly reflected the difference in
196 photosynthetic capacity of the different crops.

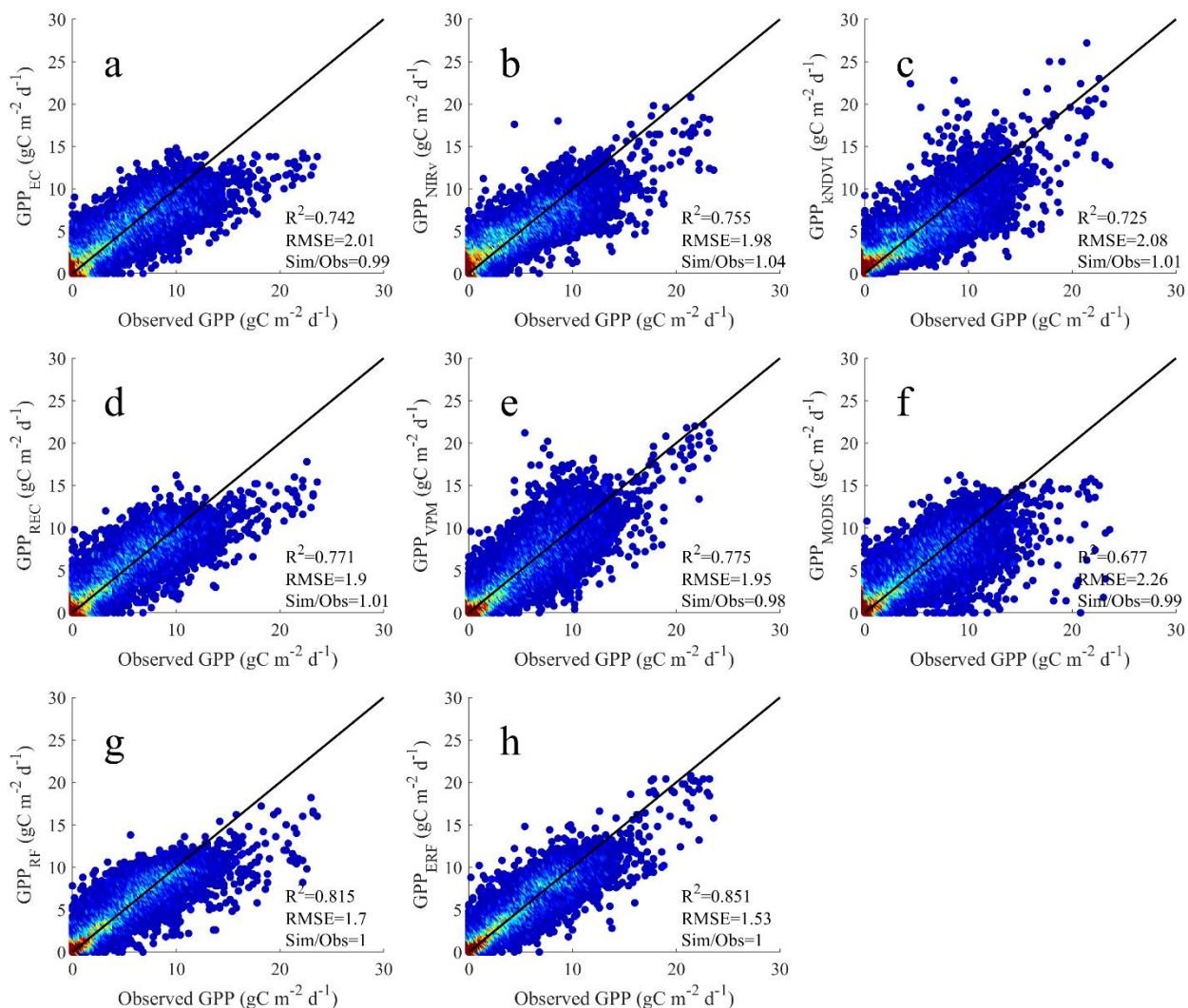
197 Figure 1 shows the performance of all models across different vegetation types. Overall, the performance of the ERF model
198 was better than that of the other GPP estimate models. GPP_{ERF} had the higher accuracy among all models, with R^2 between
199 0.61-0.91 and RMSE between 0.72-2.78 $gC\ m^{-2}\ d^{-1}$. In contrast, the LUE and vegetation index models performed slightly
200 weaker, especially in EBF, where R^2 was both below 0.5. It is worth noting that compared to other vegetation types, the
201 RMSE was highest for cropland, with 6 out of 8 models for C4 crops exceeding 3 $gC\ m^{-2}\ d^{-1}$, suggesting that these existing
202 GPP estimate models may not properly capture the seasonal changes in cropland GPP. The six models with calibrated
203 parameters and ERF model were found to have no significant deviation across vegetation types. However, GPP_{RF} was
204 significantly underestimated for C4 crops and overestimated for SHR.

a**b****c**

206 **Figure 1.** The performance of the eight models on different vegetation types. a, b and c represent R^2 , RMSE, and Sim/Obs respectively.

207 Combining the results of all flux sites, GPP_{ERF} explained 85.1% of the monthly GPP variations, while the seven GPP
208 estimate models only explained 67.7%-81.5% of the monthly GPP variations (Figure 2). Another validation method in which
209 the validation data were not selected randomly but instead sites were entirely used for either training or validation also
210 showed similar results, the average R^2 and RMSE of 200 validation results of ERF model were 0.822 and 1.68 $gC\ m^{-2}\ d^{-1}$,
211 which were obviously better than other models (Figure S3). In order to further prove the robustness of the ERF model, we
212 also used GPP estimate models with original parameters for modeling and validation. As shown in Figure S4, the
213 performance of these GPP estimate models decreased significantly, with R^2 ranging from 0.570 to 0.719 and RMSE ranging
214 from 2.29 to 3.81 $gC\ m^{-2}\ d^{-1}$. The phenomenon of "high value underestimation and low value overestimation" was also
215 pronounced. However, the ERF model maintained a consistent advantage, with R^2 significantly higher than other GPP
216 estimate models (0.856). In addition, we tested the effect of the number of GPP estimate models on the accuracy of the ERF
217 model. As shown in Table S8, as the number of GPP in the ERF model increased, the performance gain of the model
218 gradually decreased.

219 In summary, GPP_{ERF} showed high accuracy in terms of vegetation type and the ability to interpret monthly variations in GPP,
220 which also illustrates the potential of the ERF model to improve GPP estimate. However, it was observed that most GPP
221 simulations exhibited the phenomenon of "high value underestimation and low value overestimation". For example, GPP_{EC} ,
222 GPP_{REC} , GPP_{MODIS} and GPP_{RF} showed obvious underestimation in the months when the monthly GPP value surpassed 15 gC
223 $m^{-2}\ d^{-1}$ (Figure 2). Therefore, it is necessary to evaluate the performance of different models in each month and different
224 subvalues.



225

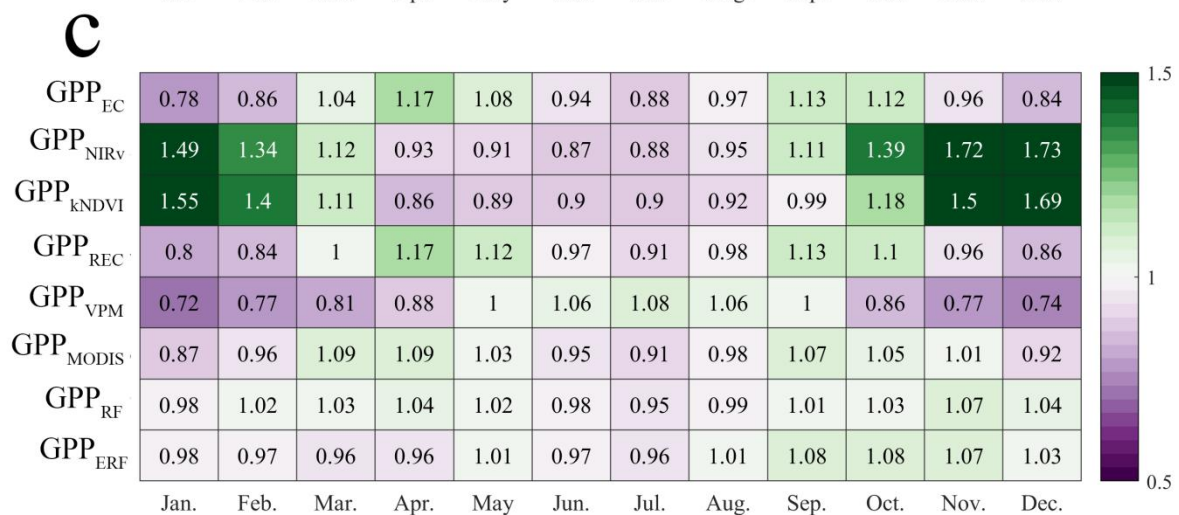
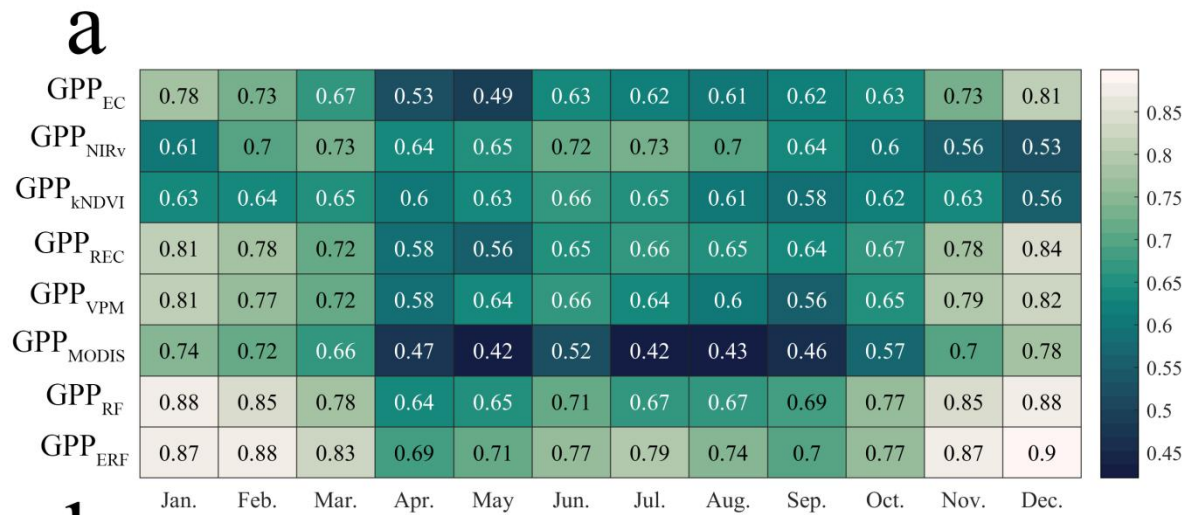
226 **Figure 2.** Comparison between the GPP simulations of the eight models and the GPP observations. a-h represents GPP_{EC}, GPP_{NIRv},
 227 GPP_{KNDVI}, GPP_{REC}, GPP_{VPM}, GPP_{MODIS}, GPP_{RF}, GPP_{ERF}, respectively.

228

229 3.2 Performance of GPP estimate models in each month and different subvalues

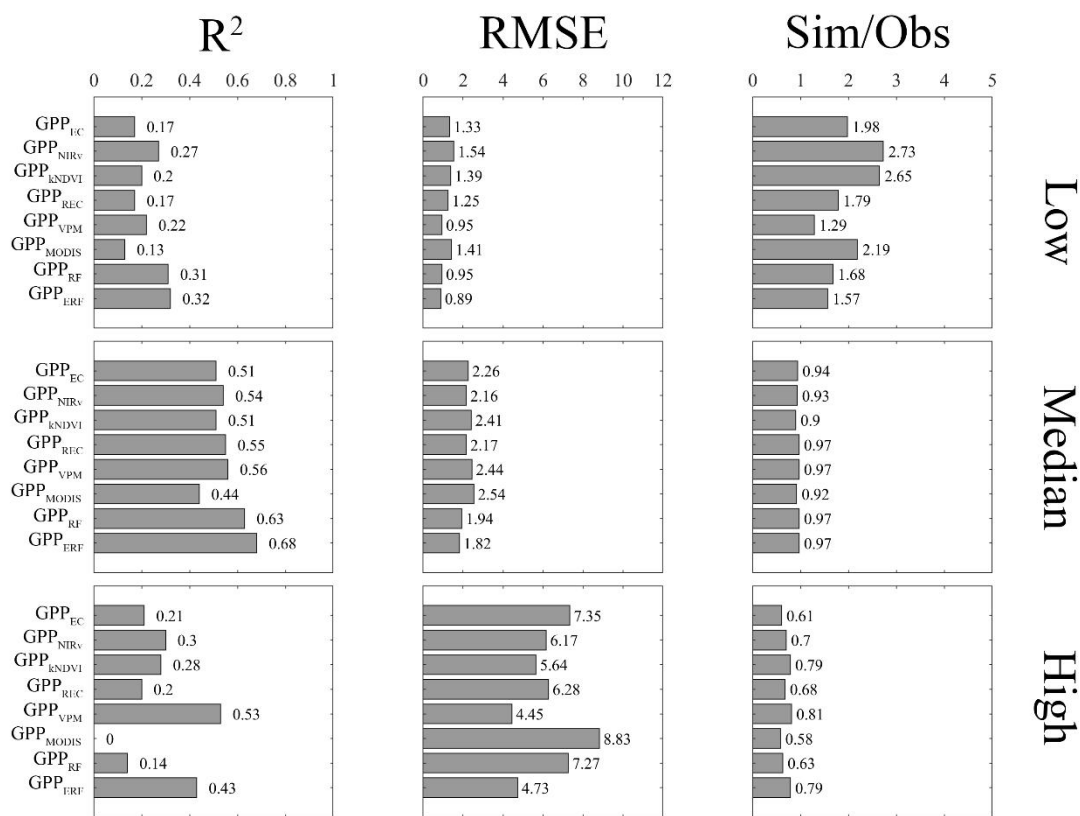
230 Figure 3 shows the simulation accuracy of the eight models in each month. The ERF model maintained a higher accuracy
 231 than other GPP estimate models, with GPP_{ERF} consistently achieving higher R^2 and lower RMSE in most months, and no
 232 evident phenomena of "high value underestimation and low value overestimation". In contrast, the accuracy of other GPP
 233 estimate models was less satisfactory accuracy, especially during winter (most flux sites are concentrated in the Northern

234 Hemisphere), the LUE models tended to underestimate GPP, and the Sim/Obs remained at 0.72-1.01, although R^2 were
235 above 0.7. Meanwhile, the vegetation index models overestimated GPP, Sim/Obs remained at 1.34-1.73, and R^2 were
236 relatively low, mostly around 0.6.



238 **Figure 3.** Performance of the eight models in each month. a, b and c represent R^2 , RMSE, and Sim/Obs respectively.

239 We further compared the performance of all models in different subvalues, including high value ($GPP > 15 \text{ gC m}^{-2} \text{ d}^{-1}$),
 240 median value ($15 \text{ gC m}^{-2} \text{ d}^{-1} > GPP > 2 \text{ gC m}^{-2} \text{ d}^{-1}$), low value ($GPP < 2 \text{ gC m}^{-2} \text{ d}^{-1}$). For extreme values, most models
 241 performed poorly (Figure 4), with R^2 for GPP estimate models falling below 0.3, and only GPP_{VPM} showing better
 242 performance in the high value. GPP_{ERF} demonstrated some improvement in both low and high values, with R^2 0.32 and 0.43,
 243 RMSE of 0.89 and 4.73 $\text{gC m}^{-2} \text{ d}^{-1}$, and Sim/Obs closer to 1, respectively. In the median value, all models performed better,
 244 with no significant bias in the GPP estimate. The R^2 of GPP estimate models ranged from 0.44 to 0.68, and the RMSE
 245 remained between 1.82 and 2.54 $\text{gC m}^{-2} \text{ d}^{-1}$. Further analysis was made at two typical sites, it was obvious that GPP_{EC} ,
 246 GPP_{REC} and GPP_{MODIS} on CN-Qia exhibited obvious underestimation during the growing season (Figure S5). On CH_Lae,
 247 GPP_{kNDVI} and GPP_{VPM} were significantly overestimated (Figure S6). In contrast, at both sites, GPP_{ERF} was more consistent
 248 with observations.



249

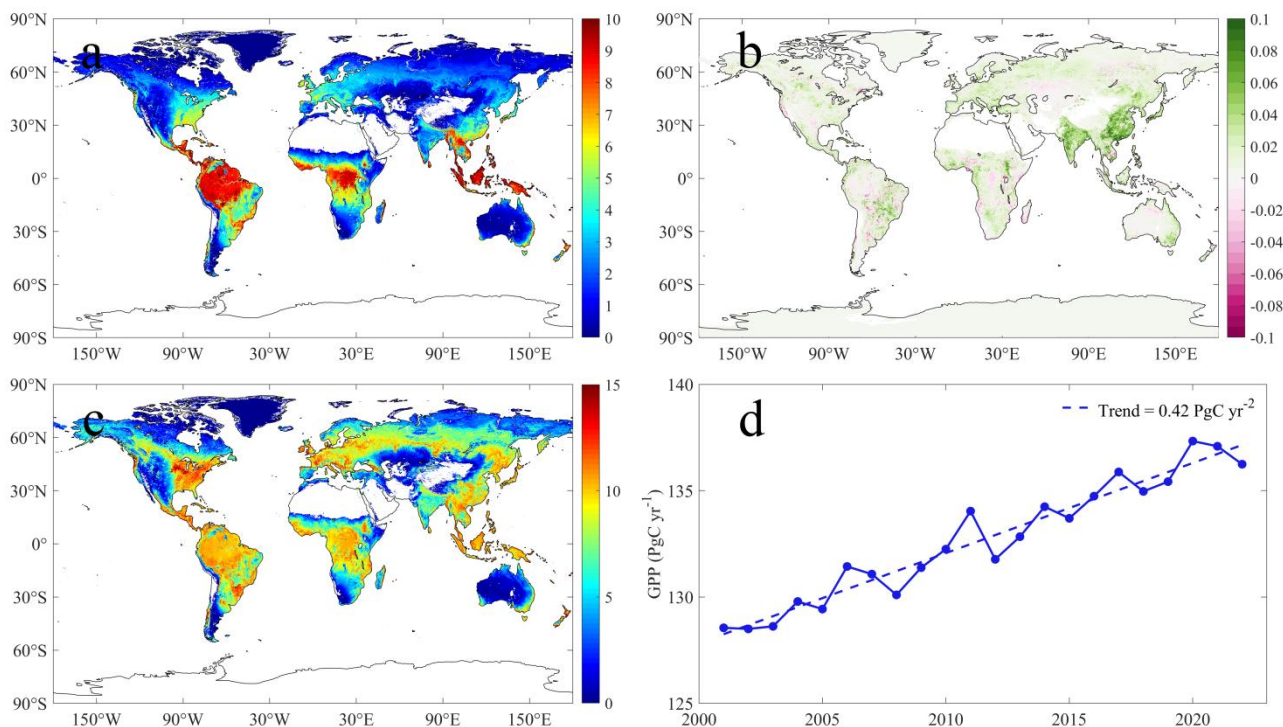
250 **Figure 4.** Performance of eight models in different subvalues.

251 3.3 Temporal and spatial characteristics of ERF_GPP and its generalization evaluation

252 Figure 5a shows the spatial distribution of the multi-year average of ERF_GPP. The high values of GPP were mainly
253 concentrated in tropical areas, exceeding $10 \text{ gC m}^{-2} \text{ d}^{-1}$, and relatively high in southeastern North America, Europe and
254 southern China, about $4\text{-}6 \text{ gC m}^{-2} \text{ d}^{-1}$. From 2001-2022, China and India showed the fastest increase in GPP, mostly at 0.1 gC
255 $\text{m}^{-2} \text{ d}^{-1}$ (Figure 5b), similar to a previous study that reported that China and India led the global greening (Chen et al., 2019).
256 We further investigated the annual maximum GPP, as shown in Figure 5c, and the North American corn belt was the global
257 leader in GPP at more than $15 \text{ gC m}^{-2} \text{ d}^{-1}$, compared to only $10 \text{ gC m}^{-2} \text{ d}^{-1}$ in most tropical forests. In 2001-2022, the global
258 GPP was $132.7 \pm 2.8 \text{ PgC yr}^{-1}$, with an increasing trend of 0.42 PgC yr^{-2} (Figure 5d). The lowest value was $128.6 \text{ PgC yr}^{-1}$ in
259 2001, and the highest value was $136.2 \text{ PgC yr}^{-1}$ in 2020.

260 The results of the two uncertainty analyses consistently indicated that ERF_GPP exhibited higher uncertainty in tropical
261 regions (Figures S7 and S8), and the uncertainty of ERF_GPP caused by the number of GPP observations was relatively
262 small, the standard deviation of 100 simulations was about $0.3 \text{ gC m}^{-2} \text{ d}^{-1}$ in the tropics and lower in other regions, below 0.1
263 $\text{gC m}^{-2} \text{ d}^{-1}$. In contrast, the uncertainty of ERF_GPP caused by the number of features was more pronounced, especially
264 when fewer features were included in the model. It is worth noting that when the number of features was five, the
265 uncertainty was already substantially less, and the standard deviation was generally lower than $0.5 \text{ gC m}^{-2} \text{ d}^{-1}$.

266



267

268 **Figure 5.** Spatial and temporal characteristics of ERF_GPP during 2001-2022. a represents the multi-year average, b represents the trend,
269 c represents the multi-year average of the annual maximum, and d represents the interannual change of GPP.

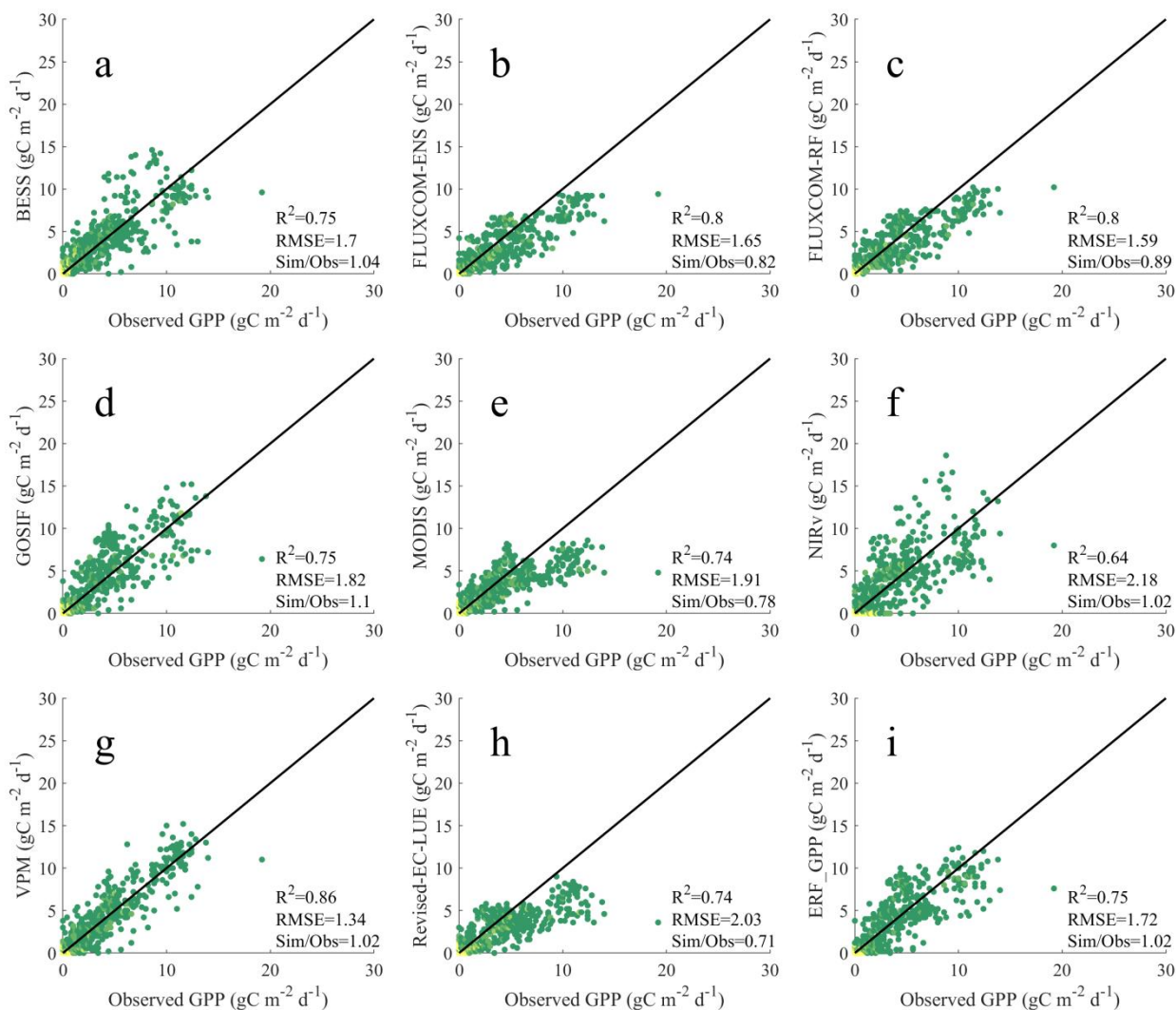
270

271 As shown in Figure 6, ERF_GPP and other GPP datasets were validated using GPP observations from ChinaFlux. Among all
272 models, VPM demonstrated the best performance, with R^2 of 0.86 and RMSE of $1.34 \text{ gC m}^{-2} \text{ d}^{-1}$. ERF_GPP also exhibited
273 high generalization, with R^2 of 0.75, RMSE of $1.72 \text{ gC m}^{-2} \text{ d}^{-1}$, there was no “high value underestimation and low value
274 overestimation”, which was comparable to the accuracy of BESS and GOSIF. However, the simulation accuracy of the other
275 GPP datasets in Chinaflux was relatively poor, with the R^2 of NIRv being only 0.64, while FLUXCOM-ENS,
276 FLUXCOM-RF, MODIS and Revised EC-LUE were significantly underestimated, with the Sim/Obs being only 0.71-0.89.
277 In the validation of FLUXNET, the R^2 of FLUXCOM-ENS, MODIS, and Revised EC-LUE ranged from 0.57 to 0.67, and
278 the RMSE ranged from 2.67 to $3.30 \text{ gC m}^{-2} \text{ d}^{-1}$, and exhibited different degrees of underestimation (Figure S9). Other GPP
279 datasets demonstrated similar performance, with ERF_GPP being the best ($R^2 = 0.74$, $\text{RMSE} = 2.26 \text{ gC m}^{-2} \text{ d}^{-1}$).

280

281

282



283

284 **Figure 6.** Comparison between the GPP datasets and the GPP observations from ChinaFlux. a-i represents BESS, FLUXCOM-ENS,
 285 FLUXCOM-RF, GOSIF, MODIS, NIRv, VPM, Revise-EC-LUE, ERF_GPP, respectively.

286 4 Discussion

287 4.1 Performance analysis of different models

288 After parameter calibration, both LUE and vegetation index models obtained reliable model accuracy. However, noticeable
 289 errors persist in different months and subvalues, indicating the prevalent phenomenon of "high value underestimation and
 290 low value overestimation" (Figures 1-4). In addition to MODIS, the GPP simulated by the other three LUE models is
 291 generally underestimated in winter (Figure 3), which may be caused by biases in the parameters used in meteorological

292 constraints. In the expression form of the temperature constraint adopted by LUE models, the maximum temperature,
293 minimum temperature and optimum temperature for limiting photosynthesis are all constants, however these values may not
294 be fixed (Grossiord et al., 2020; Huang et al., 2019). A previous study has demonstrated that the GPP estimate could be
295 effectively improved by using dynamic temperature parameters (Chang et al., 2021). Moreover, the form of meteorological
296 constraint is also an important influencing factor. Compared with other LUE models, VPM does not use VPD constraints,
297 but incorporates land surface water index from satellite observations as constraints (Xiao et al., 2004), which may be the
298 reason why the model performs better than other models at high value (Figure 4). Conversely, the two vegetation index
299 models overestimated GPP in winter, and even overestimated by 70% in December. The vegetation index model does not
300 consider meteorological constraints that believe that all environmental impacts on vegetation have been included in the
301 vegetation indices (kNDVI, NIRv) (Badgley et al., 2017; Camps-Valls et al., 2021). However, it is a fact that under high
302 temperature or low radiation, the vegetation index may still maintain the appearance of high photosynthesis (greening), while
303 in fact the GPP is low (Chen et al., 2024; Doughty et al., 2021; Yang et al., 2018). Furthermore, the relationship between
304 these vegetation indices and GPP is not robust, and the vegetation indices based on reflectance may have hysteresis (Wang et
305 al., 2022).

306 Compared to other GPP estimate models, the ERF model demonstrated better performance ($R^2 = 851$). Since there are no
307 physical constraints, the machine learning model needs to find the relationship between explanatory variables and target
308 variable from a large amount of training data (such as $GPP=f(LAI, T, P, \text{etc.})$) (Guo et al., 2023; Jung et al., 2020).
309 Therefore, the reliability of the model usually depends on the representativeness of the training data. For example, LAI can
310 explain GPP to a large extent, while complex modeling relationships are still needed from LAI to GPP. The difference
311 between the ERF model and the RF model lies in the explanatory variables. The ERF model uses multiple GPP simulations
312 that are more representative and aligned with the target variable, thus making the GPP simulations more accurate. In other
313 words, the ERF model does not need to take into account the uncertainties of the model structure (such as meteorological
314 constraints) and model parameters (such as maximum light use efficiency), but rather focuses on the uncertainties inherent in
315 the simulated GPP. To further clarify the impact of explanatory variables on the ERF model, we conducted a feature
316 importance analysis (Figure S10). From an average of 200 times, the results of the ERF model did not depend on a single
317 GPP simulation. Even GPP_{MODIS} , with the highest relative importance, accounted for no more than 25%, suggesting that the
318 ERF model behaves more like a weighted average of multiple GPP simulations. In addition, it is important to emphasize that
319 the accuracy of the ERF model is still robust even for GPP simulations of original parameters (Figure S4), which means that
320 we can try to use this method to integrate the currently published GPP data sets to obtain a more accurate global GPP
321 estimate.

322 It is worth noting that in the study of Tian et al. (2023), the ERF model was also used to improve the GPP estimate. Our
323 study extends this work in several ways. Firstly, parameter calibration was carried out in our study so that the final validation
324 results are comparable, that is, differences in model performance are mainly due to the uncertainty of the model structure.
325 Secondly, our study focused on the phenomenon of "high value underestimation and low value overestimation" of GPP

326 estimate models, with results indicating that the ERF model performed well across various vegetation types, months, and
327 subvalues. Finally, we generated the ERF_GPP dataset and validated it on different observational datasets, further
328 confirming the robustness of the ERF model in GPP estimate.

329 **4.2 Robustness of ERF_GPP**

330 Due to the inherent advantages of the RF method, the accuracy of the model was comparable to that of the ERF model, even
331 if a very simple model that used longitude, latitude, month, and year as explanatory variables (Figure S11 a). However, the
332 global GPP estimated by this model was not reliable (Figure S11 b). This illustrates that an excellent model performance
333 based on the FLUXNET sites does not necessarily imply an equivalent prediction skill in other regions. ERF model can
334 overcome this limitation to some extent. On the one hand, the explanatory variables used in the model are derived from GPP
335 simulation in which contain a lot of remote sensing information, which can ensure that the global GPP estimated by the
336 model is reliable. On the other hand, the second validation method also further shows that the ERF model has good
337 generalization and has greater potential than other models in estimating global GPP.

338 Since the current GPP datasets are generated based on remote sensing data and FLUXNET GPP observations, there is a
339 strong similarity in spatial distribution among all GPP datasets. Therefore, the validation of GPP observations independent of
340 FLUXNET is crucial. Validation results from GPP observations of ChinaFlux indicated that ERF_GPP exhibited good
341 generalization in China ($R^2=0.75$), which was slightly lower than the accuracy of 5-fold-cross-validation during modeling,
342 possibly due to the mismatch between the 0.05° GPP estimate and the footprint of the flux tower (Chu et al., 2021). In
343 addition, the validation of FLUXNET further confirms the reliability of ERF_GPP. Overall, this is comparable to or slightly
344 better than the simulation accuracy of current mainstream GPP datasets. We also observed a clear improvement in the spatial
345 maximum value of ERF_GPP in some corn growing regions, such as the North American Corn Belt (Figure 5c), which is
346 supported by previous studies showing that C4 crops have much higher GPP peaks than other vegetation types (Chen et al.,
347 2011; Yuan et al., 2015).

348 Due to the increasing drought trend, the constraining effect of water on vegetation is gradually increasing, and some studies
349 have reported the decoupling phenomenon of LAI and GPP under some specific conditions (Hu et al., 2022; Jiao et al., 2021).
350 However, in China and India with significant greening, GPP continues to increase in most datasets, and ERF_GPP supports
351 this view. This phenomenon may be attributed to the low drought pressure on croplands in China and India due to irrigation,
352 which poses less constraint on GPP (Ai et al., 2020; Ambika and Mishra, 2020). The global estimate of ERF_GPP is $132.7 \pm$
353 2.8 PgC yr^{-1} , which is close to estimates from most previous studies (Badgley et al., 2019; Wang et al., 2021). A study have
354 suggested that global GPP may reach 150-175 PgC yr^{-1} (Welp et al., 2011), however, there is no further evidence to support
355 this view.

356 ERF_GPP exhibited higher uncertainty in tropical regions, similar reports have been made in previously published GPP
357 datasets (Badgley et al., 2019; Guo et al., 2023). The scarcity of flux observations in these regions (Pastorello et al., 2020),
358 coupled with the well-known issue of cloud pollution and saturation in remote sensing data (Badgley et al., 2019),

359 exacerbates the uncertainty in GPP estimates for these regions. Therefore, in future studies, on the one hand, more flux
360 observations in tropical regions are needed, and on the other hand, attempts can be made to combine optical and microwave
361 data to improve GPP estimate.

362 **4.3 Limitations and uncertainties**

363 In this study, we improved GPP estimate based on the ERF model. Nonetheless, there are still some limitations and
364 uncertainties due to the availability of data and methods. First, C4 crop distribution maps were used in our study to improve
365 estimates of cropland GPP. However, this dataset only represents the spatial distribution of crops around the year 2000,
366 which introduce uncertainty into GPP simulations of cropland in a few C3 and C4 alternating areas. Secondly, the ERF
367 model considers six GPP simulations, and it is not clear whether adding more GPP simulations to the model can further
368 improve the GPP estimate. Finally, our model did not consider the effect of soil moisture on GPP, and some previous studies
369 have highlighted the importance of incorporating soil moisture in GPP estimates, especially for dry years (Stocker et al.,
370 2018; Stocker et al., 2019).

371 **5 Conclusion**

372 In this study, we compared the performance of the ERF model with other GPP estimate models at the site scale, especially
373 for the phenomenon of "high value underestimation and low value overestimation", and further developed the ERF_GPP
374 dataset. Overall, GPP_{ERF} had higher model accuracy, explaining 85.1% of the monthly GPP variations, and demonstrated
375 reliable accuracy in different months, vegetation types and subvalues. Over the period from 2001 to 2022, the global
376 estimate of ERF_GPP was 132.7 ± 2.8 PgC yr⁻¹, corresponding to an increasing trend of 0.42 PgC yr⁻². Validation results
377 from ChinaFlux indicated that ERF_GPP had good generalization. For the current emerging GPP estimate models, the ERF
378 model provides an alternative method that lead to better model accuracy.

379 **Data and code availability**

380 The ERF_GPP for 2001-2022 is available at <https://doi.org/10.6084/m9.figshare.24417649> (Chen et al., 2023). The spatial
381 resolution of ERF_GPP is 0.05° and the temporal resolution is monthly. Code is available from the author upon reasonable
382 request.

383 **Author contributions**

384 X.C. and T.X.C. conceived the scientific ideas and designed this research framework. X.C. compiled the data, conducted
385 analysis, prepared figures. X.C., T.X.C. and Y.F.C. wrote the manuscript. D.X.L., R.J.G., J.D., and S.J.Z. gave constructive
386 suggestions for improving the manuscript.

387 **Financial support**

388 This study was supported by the National Natural Science Foundation of China (No. 42130506, 42161144003 and 31570464)
389 and the Postgraduate Research & Practice Innovation Program of Jiangsu Province (No. KYCX23_1322).

390 **Acknowledgments**

391 We thank the two anonymous reviewers and the associate editor (Anja Rammig) for their thoughtful comments and help
392 with this study.

393 **Competing interests**

394 The contact author has declared that none of the authors has any competing interests.

395 **References**

- 396 Ai, Z. et al., 2020. Variation of gross primary production, evapotranspiration and water use efficiency for global croplands.
397 *Agricultural and Forest Meteorology*, 287.
- 398 Ambika, A.K. and Mishra, V., 2020. Substantial decline in atmospheric aridity due to irrigation in India. *Environmental*
399 *Research Letters*, 15(12).
- 400 Anav, A. et al., 2015. Spatiotemporal patterns of terrestrial gross primary production: A review. *Reviews of Geophysics*,
401 53(3): 785-818.
- 402 Badgley, G., Anderegg, L.D., Berry, J.A. and Field, C.B., 2019. Terrestrial gross primary production: Using NIRV to scale
403 from site to globe. *Global change biology*, 25(11): 3731-3740.
- 404 Badgley, G., Field, C.B. and Berry, J.A., 2017. Canopy near-infrared reflectance and terrestrial photosynthesis. *Science*
405 *advances*, 3(3): e1602244.
- 406 Bai, Y. et al., 2021. On the use of machine learning based ensemble approaches to improve evapotranspiration estimates
407 from croplands across a wide environmental gradient. *Agricultural and Forest Meteorology*, 298: 108308.
- 408 Belgiu, M. and Drăguț, L., 2016. Random forest in remote sensing: A review of applications and future directions. *ISPRS*
409 *journal of photogrammetry and remote sensing*, 114: 24-31.
- 410 Camps-Valls, G. et al., 2021. A unified vegetation index for quantifying the terrestrial biosphere. *Science Advances*, 7(9):
411 eabc7447.
- 412 Chang, Q. et al., 2021. Assessing variability of optimum air temperature for photosynthesis across site-years, sites and
413 biomes and their effects on photosynthesis estimation. *Agricultural and Forest Meteorology*, 298.
- 414 Chen, C. et al., 2019. China and India lead in greening of the world through land-use management. *Nature Sustainability*,
415 2(2): 122-129.
- 416 Chen, T., Van Der Werf, G., Gobron, N., Moors, E. and Dolman, A., 2014. Global cropland monthly gross primary
417 production in the year 2000. *Biogeosciences*, 11(14): 3871-3880.
- 418 Chen, T., van der Werf, G.R., Dolman, A.J. and Groenendijk, M., 2011. Evaluation of cropland maximum light use
419 efficiency using eddy flux measurements in North America and Europe. *Geophysical Research Letters*, 38.
- 420 Chen, X. et al., 2024. Vegetation Index - Based Models Without Meteorological Constraints Underestimate the Impact of
421 Drought on Gross Primary Productivity. *Journal of Geophysical Research: Biogeosciences*, 129(1):
422 e2023JG007499.

423 Chen, Y., Yuan, H., Yang, Y. and Sun, R., 2020. Sub-daily soil moisture estimate using dynamic Bayesian model averaging.
424 *Journal of Hydrology*, 590: 125445.

425 Chu, H. et al., 2021. Representativeness of Eddy-Covariance flux footprints for areas surrounding AmeriFlux sites.
426 *Agricultural and Forest Meteorology*, 301: 108350.

427 Dechant, B. et al., 2022. NIRVP: A robust structural proxy for sun-induced chlorophyll fluorescence and photosynthesis
428 across scales. *Remote Sensing of Environment*, 268: 112763.

429 Dechant, B. et al., 2020. Canopy structure explains the relationship between photosynthesis and sun-induced chlorophyll
430 fluorescence in crops. *Remote Sensing of Environment*, 241: 111733.

431 Doughty, R. et al., 2021. Small anomalies in dry-season greenness and chlorophyll fluorescence for Amazon moist tropical
432 forests during El Nino and La Nina. *Remote Sensing of Environment*, 253.

433 Grossiord, C. et al., 2020. Plant responses to rising vapor pressure deficit. *New Phytologist*, 226(6): 1550-1566.

434 Guo, R. et al., 2023. Estimating Global GPP From the Plant Functional Type Perspective Using a Machine Learning
435 Approach. *Journal of Geophysical Research-Biogeosciences*, 128(4).

436 Hersbach, H. et al., 2020. The ERA5 global reanalysis. *Quarterly Journal of the Royal Meteorological Society*, 146(730):
437 1999-2049.

438 Hu, Z. et al., 2022. Decoupling of greenness and gross primary productivity as aridity decreases. *Remote Sensing of
439 Environment*, 279: 113120.

440 Huang, M. et al., 2019. Air temperature optima of vegetation productivity across global biomes. *Nature ecology & evolution*,
441 3(5): 772-779.

442 Jiao, W. et al., 2021. Observed increasing water constraint on vegetation growth over the last three decades. *Nature
443 Communications*, 12(1).

444 Jung, M. et al., 2020. Scaling carbon fluxes from eddy covariance sites to globe: synthesis and evaluation of the FLUXCOM
445 approach. *Biogeosciences*, 17(5): 1343-1365.

446 Li, B. et al., 2023. BESSv2.0: A satellite-based and coupled-process model for quantifying long-term global
447 land-atmosphere fluxes. *Remote Sensing of Environment*, 295.

448 Li, X. and Xiao, J., 2019. A Global, 0.05-Degree Product of Solar-Induced Chlorophyll Fluorescence Derived from OCO-2,
449 MODIS, and Reanalysis Data. *Remote Sensing*, 11(5).

450 Monfreda, C., Ramankutty, N. and Foley, J.A., 2008. Farming the planet: 2. Geographic distribution of crop areas, yields,
451 physiological types, and net primary production in the year 2000. *Global Biogeochemical Cycles*, 22(1).

452 Pastorello, G. et al., 2020. The FLUXNET2015 dataset and the ONEFlux processing pipeline for eddy covariance data.
453 *Scientific data*, 7(1): 1-27.

454 Pei, Y. et al., 2022. Evolution of light use efficiency models: Improvement, uncertainties, and implications. *Agricultural and
455 Forest Meteorology*, 317: 108905.

456 Ruehr, S. et al., 2023. Evidence and attribution of the enhanced land carbon sink. *Nature Reviews Earth & Environment*,
457 4(8): 518-534.

458 Running, S.W. et al., 2004. A continuous satellite-derived measure of global terrestrial primary production. *Bioscience*,
459 54(6): 547-560.

460 Ryu, Y., Berry, J.A. and Baldocchi, D.D., 2019. What is global photosynthesis? History, uncertainties and opportunities.
461 *Remote sensing of environment*, 223: 95-114.

462 Stocker, B.D. et al., 2018. Quantifying soil moisture impacts on light use efficiency across biomes. *New Phytologist*, 218(4):
463 1430-1449.

464 Stocker, B.D. et al., 2019. Drought impacts on terrestrial primary production underestimated by satellite monitoring. *Nature
465 Geoscience*, 12(4): 264+.

466 Tian, Z. et al., 2023. Fusion of Multiple Models for Improving Gross Primary Production Estimation With Eddy Covariance
467 Data Based on Machine Learning. *Journal of Geophysical Research: Biogeosciences*, 128(3): e2022JG007122.

468 Wang, J. et al., 2017. Decreasing net primary production due to drought and slight decreases in solar radiation in China from
469 2000 to 2012. *Journal of Geophysical Research: Biogeosciences*, 122(1): 261-278.

470 Wang, S., Zhang, Y., Ju, W., Qiu, B. and Zhang, Z., 2021. Tracking the seasonal and inter-annual variations of global gross
471 primary production during last four decades using satellite near-infrared reflectance data. *Science of the Total
472 Environment*, 755: 142569.

473 Wang, X. et al., 2022. Satellite solar-induced chlorophyll fluorescence and near-infrared reflectance capture complementary
474 aspects of dryland vegetation productivity dynamics. *Remote Sensing of Environment*, 270: 112858.

475 Welp, L.R. et al., 2011. Interannual variability in the oxygen isotopes of atmospheric CO₂ driven by El Nino.
476 *Nature*, 477(7366): 579-582.

477 Xiao, J. et al., 2019. Remote sensing of the terrestrial carbon cycle: A review of advances over 50 years. *Remote Sensing of*
478 *Environment*, 233: 111383.

479 Xiao, X. et al., 2004. Modeling gross primary production of temperate deciduous broadleaf forest using satellite images and
480 climate data. *Remote sensing of environment*, 91(2): 256-270.

481 Xu, T., White, L., Hui, D. and Luo, Y., 2006. Probabilistic inversion of a terrestrial ecosystem model: Analysis of
482 uncertainty in parameter estimation and model prediction. *Global Biogeochemical Cycles*, 20(2).

483 Yang, J. et al., 2018. Amazon drought and forest response: Largely reduced forest photosynthesis but slightly increased
484 canopy greenness during the extreme drought of 2015/2016. *Global Change Biology*, 24(5): 1919-1934.

485 Yao, Y. et al., 2017. Improving global terrestrial evapotranspiration estimation using support vector machine by integrating
486 three process-based algorithms. *Agricultural and Forest Meteorology*, 242: 55-74.

487 Yao, Y. et al., 2014. Bayesian multimodel estimation of global terrestrial latent heat flux from eddy covariance,
488 meteorological, and satellite observations. *Journal of Geophysical Research: Atmospheres*, 119(8): 4521-4545.

489 Yuan, W. et al., 2015. Uncertainty in simulating gross primary production of cropland ecosystem from satellite-based
490 models. *Agricultural and Forest Meteorology*, 207: 48-57.

491 Yuan, W. et al., 2014. Global comparison of light use efficiency models for simulating terrestrial vegetation gross primary
492 production based on the LaThuile database. *Agricultural and Forest Meteorology*, 192: 108-120.

493 Yuan, W. et al., 2007. Deriving a light use efficiency model from eddy covariance flux data for predicting daily gross
494 primary production across biomes. *Agricultural and Forest Meteorology*, 143(3-4): 189-207.

495 Yuan, W. et al., 2019. Increased atmospheric vapor pressure deficit reduces global vegetation growth. *Science advances*,
496 5(8): eaax1396.

497 Zhang, Y. et al., 2017. A global moderate resolution dataset of gross primary production of vegetation for 2000–2016.
498 *Scientific data*, 4(1): 1-13.

499 Zheng, Y. et al., 2020. Improved estimate of global gross primary production for reproducing its long-term variation,
500 1982–2017. *Earth System Science Data*, 12(4): 2725-2746.

501

502